SSSV SYMPOSIUM – 2025

21st Nov 2025, Indian Institute of Technology Hyderabad





Shizuoka University

Sanada and Mizushima Laboratory

Symposium Program (Detailed schedule)

21st Nov, Indian Institute of Technology Hyderabad

Session-1 (Chair: Anvesh)		
Time	Speaker	Торіс
10:00 AM – 10:15 AM	Toshiyuki Sanada (Shizuoka University)	Introductory speech and remarks
10:15 AM - 10:35 AM	Charul Gupta (IIT Hyderabad)	Vortex ring formation from cavitation bubble dynamics in the presence of a confined air bubble
10:35 AM - 10:55 AM	Satoi Suzuki (Shizuoka University)	The Dispersion of a Clean Spherical Bubble Chain at Intermediate Reynolds Numbers
10:55 AM - 11:15 AM	Ryo Nagao (Shizuoka University)	Effect of Wall Inclination and Wettability on Bubble Bouncing Near Porous Wall
11:15 AM - 11:30 AM	High Tea	
Session-2 (Chair: Dharanija)		
Time	Speaker	Торіс
11:30 AM - 11:50 AM	Makoto Miwa (Shizuoka University)	Liquid movement and replacement induced by the volume change of a PVA brush
11:50 AM - 12:10 AM	Edin Michael (IIT Hyderabad)	Primary Breakup Model for Annular Sheet Composed of non-Newtonian Fluid Using Linear Stability Analysis
12:10 PM - 12:30 PM	Bunta Inagaki (Shizuoka University)	Effect of liquid viscosity on liquid transport in upward vertical annular flow
12:30 PM - 2:00 PM	Lunch Break	
Session-3 (Chair: Mohana)		
Time	Speaker	Торіс
02:00 PM - 02:20 PM	Jukiya Ikegaya (Shizuoka University)	Numerical simulation of liquid film thickness distribution and liquid replacement on a rotating disk
02:20 PM - 02:40 PM	Kingshuk Mondal (IIT Hyderabad)	Study of the Atmospheric Boundary Layer Flow over a Stripe/Band heterogeneity
02:40 PM - 03:00 PM	Subhasish Guchhait (IIT Hyderabad)	Self-propelling microswimmers near the corners of a confined meniscus: Attraction, trapping, and escape
03:00 PM - 03:20 PM	Om Godse (IIT Hyderabad)	Hydrodynamics of a falling plate
03:20 PM - 03:30 PM	Karri Badarinath (IIT Hyderabad)	Concluding remarks and informal discussion
03:30 PM - 04:00 PM	High Tea	

Book Of abstracts

Vortex ring formation from cavitation bubble dynamics in the presence of a confined air bubble. (10:15~10:35)

*Charul Gupta (IIT Hyderabad), Harish Dixit & Badarinath Karri. (IIT Hyderabad)

Abstract

This study examines the formation of vortex rings resulting from the dynamics of a cavitation bubble in the presence of a confined air bubble. The cavitation bubble is generated just above a blind hole, with the air bubble confined at the bottom of the hole. Under certain parametric conditions, such a configuration results in the formation of a vortex ring that moves away from the blind hole. The entire phenomenon is captured using shadowgraphy and high-speed imaging, with machine learning and image processing algorithms employed to extract quantitative data. It is found that the dimensionless location of the cavitation bubble relative to the blind hole plays a key role in whether or not a vortex ring is formed. In experiments where vortex ring forms, two intermediate phenomena are observed: the formation of a penetrating bubble and the subsequent recoiling of the air bubble. The size of the penetrating bubble determines the intensity of the recoiling action of the air bubble, which in turn leads to the formation of the vortex ring. This study seeks to elucidate the mechanism responsible for the formation of the vortex ring and its correlation with the dimensionless location of the cavitation bubble.

The Dispersion of a Clean Spherical Bubble Chain at Intermediate Reynolds Numbers

Satoi Suzuki, Toshiyuki Sanada

Department of Mechanical Engineering, Shizuoka University 3-5-1 Johoku, Chuo-ku, Hamamatsu, Shizuoka, 432-8561 JAPAN.

Keywords: Bubble dynamics, Bubble chain, Bubble-bubble interaction, Lift force

ABSTRACT - Bubble chains, observed in a glass of champagne or a carbonated drink, exhibit various rising behavior, such as straight-line motion or dispersion. Bubble chain behavior is influenced by bubble deformation, surface contamination and bubble generation frequency, which is related to the distance between bubbles, and is associated with bubble-bubble interaction. However, it is difficult to control frequency and bubble size independently and examine the influence of bubble-bubble interaction on the behavior, while excluding deformation and contamination effects. In this study, we independently controlled frequency and bubble size using an originally developed bubble generator. To focus on the interaction effect, we generated the spherical bubble chain in clean liquid. We also constructed a bubble chain model that includes bubble-bubble interaction with multiple bubbles. The model and experimental results exhibited similar dispersion shape, indicating that the interaction is one of the primary factors of dispersion. However, a quantitative comparison revealed that the dispersion observed in the model was smaller than that in the experiment. This suggests that, in the experiment, unconsidered effects promote dispersion. We hypothesized that the effect of upward liquid flow induced by bubble chain. The upward flow generated by repeated passage of bubbles may influence the dispersion behavior. We developed the model incorporating the effect of upward flow.

1. INTRODUCTION

Bubble chains are commonly observed in a glass of champagne or a carbonated drink. When bubbles are generated from a single orifice, the bubble chain shows dispersion, widening as it rises. Atasi et al. (2023) attributed this dispersion to bubble-bubble interactions, deformation, and contamination [1]. As the bubble generation frequency increases, bubbles approach more closely, enhancing interactions and increasing dispersion. Conversely, larger or surfactant-influenced bubbles tend to reduce dispersion. However, independently controlling generation frequency and diameter making it difficult to evaluate each contribution. In this study, we focused on bubble-bubble interactions and investigated their contribution to dispersion. In the experiments, we used clean spherical bubbles to minimize deformation and contamination. Additionally, we developed a bubble chain model incorporating only bubble-bubble interactions to evaluate their influence on the dispersion.

2. EXPERIMENTAL METHOD

Figure. 1 shows the schematic of the experimental setup. We independently control the generation

frequency f and bubble diameter d by adjusting the acoustic wave. We pressurize the air inside the tube with hole using a compressor and pressure controller. We output acoustic wave from the speaker to generate bubbles through hole. We set f=4, 8, 12, and 20 Hz, and d=0.4, 0.5, and 0.6 mm. Liquids are ultrapure water and silicone oil (kinematic viscosity $\nu=1\times 10^{-6}~\text{m}^2/\text{s}$). We analysed the dispersion using dispersion angle α .

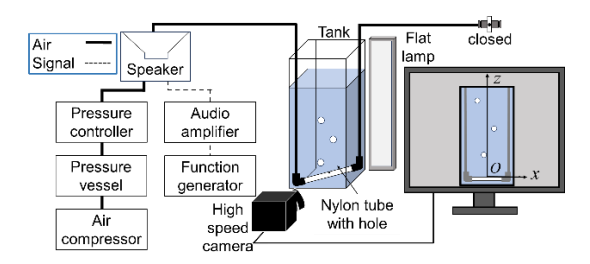


Fig. 1. Schematic of experimental setup.

3. RESULTS AND DISCUSSION

Figure. 2 shows the trajectories of bubble chains with f = 0.5 mm in silicone oil ($\nu = 1 \times 10^{-6}$ m²/s) from experiment. f is shown from left to right: f = 4, 8, 12, and 20 Hz. After generation, each bubble chains follow the linear path up to certain height and then begin to disperse. As frequency f increases, bubble chains disperse more widely and begin to disperse at lower positions.

In order to investigate the dispersion mechanism, we simulate the dispersion of bubble chain using the lagrangian model that incorporates bubble-bubble interaction. Hallez & Legendre (2011) proposed semianalytical formulation for interaction force $F_{int_{i,i}}$ coefficients acting on clean spherical bubble i due to its interaction with clean spherical bubble j [2]. We configure the model so that each generated bubble interacts with two bubbles generated earlier and later. Bubble i is subjected to interaction forces $F_{int_{i,(i-2)}}$, $\pmb{F}_{int_{i,(i-1)}}$, $\pmb{F}_{int_{i,(i+1)}}$, and $\pmb{F}_{int_{i,(i+2)}}$. Since the other bubbles are sufficiently distant, we neglect their interactions. Bubble i ascends while experiencing buoyancy \mathbf{F}_{B_i} , steady drag \mathbf{F}_{QS_i} , and added mass forces F_{AM_i} [3]. We solve the equations of motion (1) for each bubble and track the bubble dynamics.

$$\frac{\pi}{6} \rho_G R^3 \frac{d\mathbf{U}_i}{dt} = \mathbf{F}_{B_i} + \mathbf{F}_{QS_i} + \mathbf{F}_{AM_i} + \mathbf{F}_{int_{i,(i-2)}} + \mathbf{F}_{int_{i,(i-1)}} + \mathbf{F}_{int_{i,(i+1)}} + \mathbf{F}_{int_{i,(i+2)}}.$$
 (1)

Here, ρ_G is gas density, and U_i is bubble i velocity. We randomly assigned the x-coordinate of each bubble when generated within the range 0 < x < 0.01 mm.

Figure. 3 shows the trajectories of models with d = 0.5 mm in silicone oil ($v = 1 \times 10^{-6}$ m²/s). Consistent with the experimental results, as f increases, bubble chains disperse more widely and begin to disperse at lower positions. However, quantitative comparison shows that the different dispersion behavior between experimental results and models.

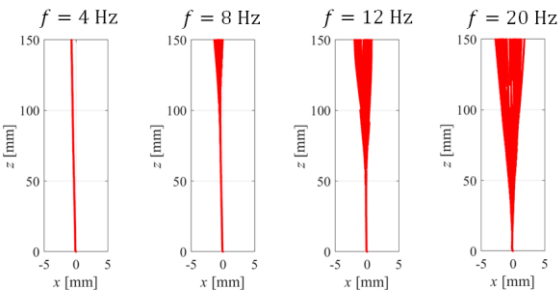


Fig. 2. Trajectories of bubbles in experiment.

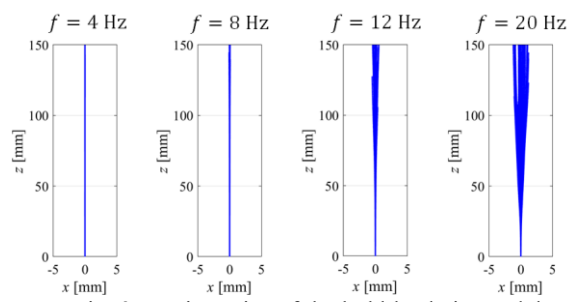


Fig. 3. Trajectories of the bubble chain model.

Figure. 4 shows the relationship between the dispersion angle α and f. Experimental results and the model are plotted with colored markers and cross (x) markers respectively. The model underestimates α compared to the experiment.

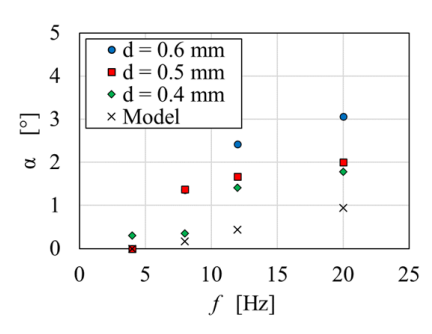


Fig. 4. Relationship between dispersion angle α and generation frequency f.

Therefore, we consider that unaccounted effects contribute to the bubble chain dispersion in addition to bubble-bubble interaction. As one of the unaccounted effects, the liquid flow fields induced by the rising bubble chain may be a contributing factor, as illustrated in Fig. 5. A bubble chain repeatedly passes the same area in the liquid and generate the upward flow with velocity gradient. We consider that the velocity gradient of upward flow contributes the dispersion. We incorporate the effect of the upward flow into the model. The

equations of motion for bubble i is modified as follows:

$$\frac{\pi}{6} \rho_G R^3 \frac{d\mathbf{U}_i}{dt} = \mathbf{F}_{B_i} + \mathbf{F}_{QS_i} + \mathbf{F}_{AM_i} + \mathbf{F}_{int_{i,(i-2)}}
+ \mathbf{F}_{int_{i,(i-1)}} + \mathbf{F}_{int_{i,(i+1)}} + \mathbf{F}_{int_{i,(i+2)}} + \mathbf{F}_{LUF_i}.$$
(2)

We additionally introduced a new lift force \mathbf{F}_{LUF_i} acting on bubble i induced by the velocity gradient of upward flow. Here, we defined \mathbf{F}_{LUF_i} using classical formulation that represents the lift force experienced by a spherical bubble, as follows [4]:

$$\mathbf{F}_{LUF_i} = C_{LUF} \rho_L \frac{\pi d^3}{6} (\mathbf{V}_L - \mathbf{U}_i) \times (\nabla \times \mathbf{V}_L)$$
 (3)

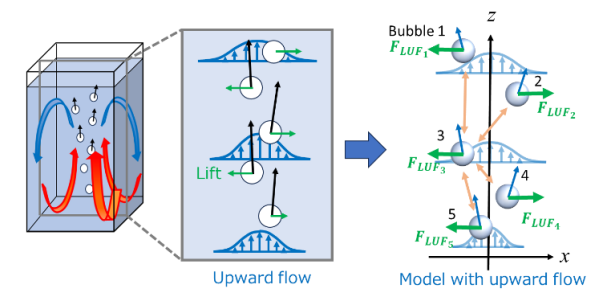


Fig. 5. The upward flow induced by a bubble chain.

Figure. 6 shows the trajectories of models, incorporating the upward flow effect, calculated by equations (2) with d = 0.5 mm in silicone oil ($\nu = 1 \times 10^{-6}$ m²/s). The introduction of the upward flow led to an increase in dispersion at f = 12, and 20 Hz.

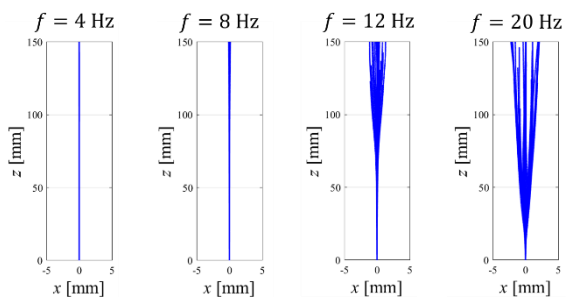


Fig. 6. Trajectories of the bubble chain model incorporating the upward flow effect.

4. CONCLUSION

In this study, we investigated clean spherical bubble chains through both experimental and modeling approaches. The results indicate that while bubble—bubble interactions are the primary factor of dispersion in the bubble chain, unaccounted effects also influence the dispersion.

- [1] Atasi, O., Ravisankar, M., Legendre, D. and Zenit, R., Physical Review Fluids, 8(5), 053601 (2023).
- [2] Hallez, Y., & Legendre, D., J. Fluid Mechanics, 673, 406-431 (2011).
- [3] Maeda, K., Date, M., Sugiyama, K., Takagi, S., & Matsumoto, Y., J. Fluid Mechanics, 919, A30 (2011).
- [4] Legendre, D., & Magnaudet, J., J. Fluid Mech. 368, 81 (1998).

Effect of Wall Inclination and Wettability on Bubble Bouncing Near Porous Wall

Ryo Nagao, Toshiyuki Sanada Department of Mechanical Engineering, Shizuoka University 3-5-1 Johoku, Naka-ku, Hamamatsu, Shizuoka, 432-8561 JAPAN.

Keywords: Bubble dynamics, Inclined wall, Bubble bouncing or sliding, Porous media

ABSTRACT – Bubble behavior near wall surfaces plays an important role in multiphase flows, particularly in heat and mass transfer. This study examines how wall material properties such as wettability, porosity, and stiffness and wall inclination affect bubble motion. A single bubble was generated in ultrapure water and made to collide with polyurethane sponge, silicone rubber, PVA sponge, and glass walls inclined at 0°, 30°, and 60°. High-speed imaging was used to analyze bubble deformation, sliding/bouncing behavior, rising velocity, and trajectory.

Bubbles showed greater flattening on horizontal walls, while sliding and bouncing reduced deformation. The rising velocity decreased by about 50% during rebound, except for the porous polyurethane sponge, where the reduction was limited to about 10%. These results demonstrate that surface porosity plays a key role in bubble dynamics near inclined walls.

1. INTRODUCTION

A flow in which numerous bubbles are dispersed within a liquid is referred to as a bubbly flow. Such flows are commonly observed in everyday phenomena, such as carbonated beverages and boiling water. Bubble behavior varies depending on the properties of the continuous phase, bubble size, and bubble—bubble interactions. For example, near a wall surface, bubbles may exhibit bouncing or sliding behavior, which can influence heat transfer. However, these behaviors have not yet been fully understood.

To clarify bubble dynamics near walls, de Vries et al. [1] investigated bubble approach and bouncing, while Barbosa et al. [2] examined the transition from sliding to bouncing on inclined hydrophilic walls. Jeong et al. [3] reported that surface wettability affects zigzag bubble rising behavior near vertical walls. Although many studies have explored bubble behavior near walls, the detailed physics of the thin liquid film between the bubble and wall remains unclear, and investigations where multiple parameters are simultaneously controlled are still limited.

In this study, we focus on wall materials and investigate how surface structure, stiffness, and inclination angle influence bubble bouncing and sliding behavior.

2. EXPERIMENTAL METHOD

Figure 1 shows a schematic of the experimental setup. An acrylic tank was filled with ultrapure water, and a nylon tube with a small orifice was placed at the bottom to generate bubbles. The pressure inside the tube was controlled by supplying compressed air through a compressor and adjusting it with a pressure controller, preventing water backflow and allowing bubble size control.

The wall surface for bubble collision was fixed to the inner side of the tank using a supporting protrusion. The wall inclination angle θ_w was set to 0°, 30°, and 60°, the sliding and bouncing behaviors of bubbles were observed. Polyurethane sponge, silicone rubber, glass, and PVA sponge were used to examine the influence of wall material properties.

Bubbles were generated using acoustic excitation. A rectangular wave from a function generator was amplified and emitted as sound waves from a speaker, and the acoustic pressure transmitted through the tube induced bubble formation. Bubble motion was recorded using a high-speed camera (FASTCAM Mini WX 100) at 1080 fps with a shutter speed of 1/2160 s.

The bubble diameter was calculated in MATLAB using the following equation

$$d_{eq} = (d_{ma}^2 \cdot d_{mi})^{\frac{1}{3}} \tag{1}$$

Where d_{eq} , d_{ma} and d_{mi} are the equivalent bubble diameter, major axis length, and minor axis length, respectively. In this study, two bubble sizes were used: $d_{eq} = 2.62 \pm 0.1, 1.84 \pm 0.03, 1.19 \pm 0.05$ mm. The Reynolds numbers at these conditions were $778 \pm 48, 608 \pm 40$, and 272 ± 48 , and the Weber numbers were $4.65 \pm 0.28, 3.10 \pm 0.13$, and 2.54 ± 0.24 , respectively. The bubble aspect ratio was calculated using the following expression

$$\chi = \frac{d_{ma}}{d_{mi}} \tag{2}$$

A value of χ close to 1 indicates a nearly spherical bubble, while larger values correspond to increased deformation toward an ellipsoidal shape.

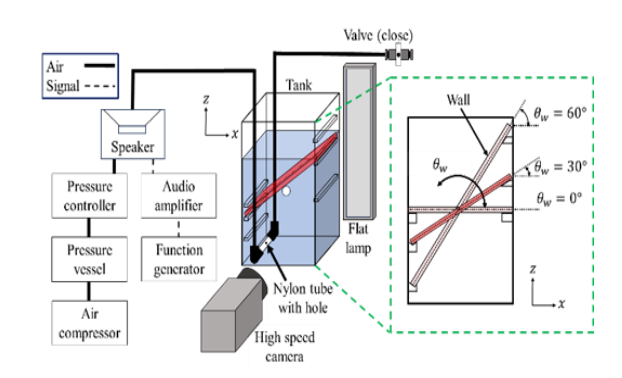


Figure 1 Schematic diagram of the experimental apparatus.

3. RESULTS AND DISCUSSION

3.1 Relationship Between Bubble Shape Change and Rising Path

Figure 2 shows the change in aspect ratio between free rising conditions and near-wall conditions. For $\theta_w = 0^\circ$, all materials exhibit $\chi < \chi_w$, indicating that the bubble becomes more flattened upon colliding with the wall. In contrast, for $\theta_w = 30^\circ$ and 60° , $\chi > \chi_w$ is observed, meaning that the bubble shape becomes closer to spherical near the wall.

Figures 3 and 4 present the bubble trajectories for $\theta_w=30^\circ$ and 60° , respectively. At $\theta_w=30^\circ$, $\chi_w\approx 1$, and a sliding motion along the wall surface is observed. In contrast, at $\theta_w=60^\circ$, $\chi_w<1$, where the bubble elongates in the direction normal to the wall and exhibits a rebound behaviour. It should be noted that χ_w is calculated based on the bubble shape at the moment of maximum flattening during wall collision for $\theta_w=0^\circ$, and at the instant when the bubble is closest to the wall during sliding for $\theta_w=30^\circ$ and 60° .

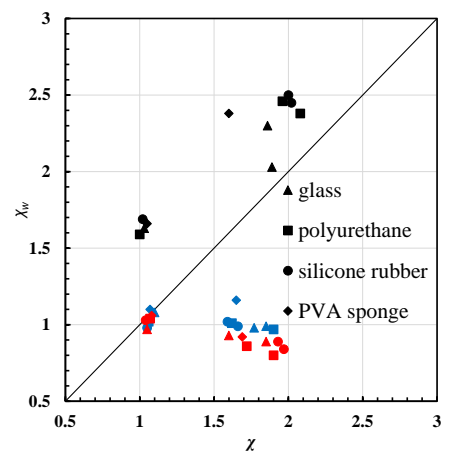


Figure 2 Change in bubble aspect ratio due to wall influence. The black, blue, and red markers represent $\theta_w = 0^\circ$, 30° , and 60° , respectively.

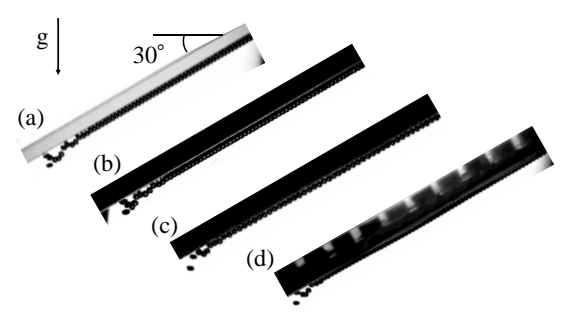


Figure 3 Bubble Trajectories at $\theta w = 30^{\circ}$ for different wall materials: (a) glass, (b) silicone rubber sheet, (c) polyurethane sponge, (d)PVA sponge.

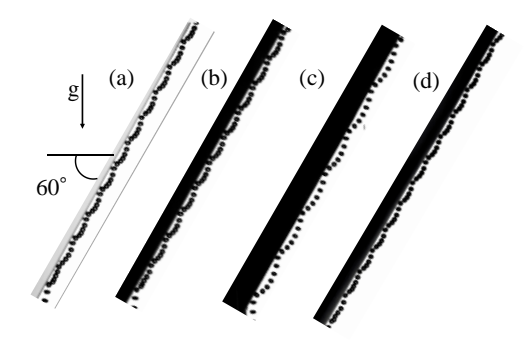


Figure 4 Bubble Trajectories at $\theta_w = 60^{\circ}$ for different wall materials.

3.2 Relationship Between Rising Velocity and Motion Path

Figure 5 shows the change in bubble rising velocity due to interaction with the wall at $\theta_w = 60^{\circ}$. Under all the rising velocity decreased approximately half of the free-rising value because of the wall influence. Notably, only the polyurethane sponge exhibited a distinct behavior, where the reduction in rising velocity was limited to about 10%. In addition, as shown in Figure 4, the bouncing behavior on the polyurethane sponge differed from that on the other materials: the bubble traveled a longer distance after rebound and the number of rebounds was smaller. In contrast, multiple rebounds were observed on glass, silicone rubber, and PVA sponge surfaces, demonstrating bouncing behavior consistent with previous reports.

In addition, when the polyurethane sponge was used, the bubble's bouncing behavior changed. Because the polyurethane sponge has a porous structure and retains liquid on its surface, it provides a boundary condition with partial slip. As a result, the bubble can slide more easily along the surface, and the reduction in rising velocity becomes smaller compared to other materials.

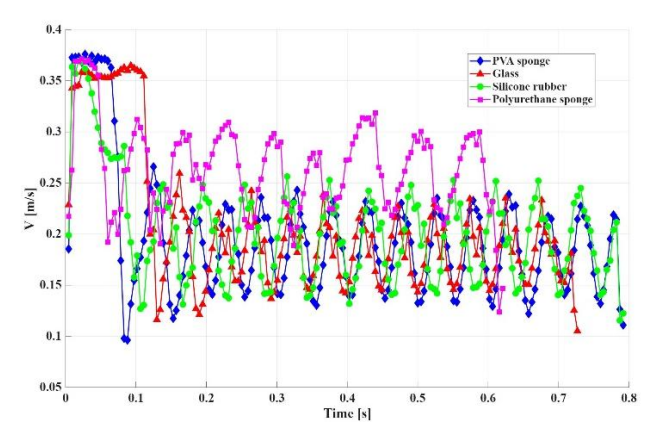


Figure 5 Decrease in rising velocity due to interaction with walls.

4. CONCLUSION

In this study, the effects of wall inclination and surface structure on bubble behavior near four different wall materials were investigated experimentally. As the inclination angle increased, the bubble shape transitioned from a flattened to an elongated form, accompanied by an increase in rising velocity. On the polyurethane wall, the decrease in velocity during bouncing was smaller than that on the other materials, resulting in a distinct bouncing behavior. These results demonstrate that bubble shape, rising velocity, and motion trajectory are strongly dependent on the inclination and surface structure of the wall.

- [1] de Vries, A. W. G., Biesheuvel, A., and van Wijngaarden, L. Int. J. Multiphase Flow, Vol. 28, 1823-1835 (2002).
- [2] Barbosa C., Legendre D., and Zenit R., Phys. Rev. Fluids Vol. 1, 032201 (2016).
- [3] Jeong. H, and Park. H, J. Fluid Mech., Vol. 771, 564-594 (2015).

Liquid movement and replacement induced by the volume change of a PVA brush

Makoto Miwa, Toshiyuki Sanada,

Department of Mechanical Engineering, Shizuoka University 3-5-1 Johoku, Chuo-ku, Hamamatsu, Shizuoka, 432-8561 JAPAN.

Keywords: Soft porous sponge, Volume change, Flow visualization, Liquid exchange, Cleaning

ABSTRACT - Polyvinyl acetal (PVA) brushes have gained widespread application in post-CMP cleaning in semiconductor manufacturing. We propose that efficient cleaning requires the prompt removal of residual slurry from the wafer surface, immediately followed by replenishment with fresh cleaning chemicals. To examine this hypothesis, we have conducted measurements of brush deformation and liquid transport through a system using the concentration difference of fluorescence [1]. In this study, the influence of the surrounding liquid level on liquid motion was analyzed using the molecular tagging approach. The findings demonstrated that when the brush experiences non-uniform deformation, liquid replacement between its inner and outer regions becomes greater, and this phenomenon is further intensified under reduced liquid levels.

1. INTRODUCTION

As semiconductor devices become increasingly complex with the adoption of multilayer structures, the demand for highly precise surface planarization continues to grow. Achieving an atomically flat surface at each layer is essential to ensure reliable interconnect formation and overall device performance. Chemical-Mechanical Planarization (CMP) is a crucial process for accomplishing a super-flat surface. Following CMP, post-CMP cleaning is necessary to maintain surface integrity and prevent defects. In these cleaning steps, PVA brushes, known for their high hydrophilicity and soft, porous structure, are widely utilized due to their excellent cleaning effectiveness. While PVA brushes effectively remove particulate contaminants, enhancing cleaning effectiveness requires more understanding of the cleaning mechanisms. We hypothesize that liquid movements such as flow-in, flow-out, and replacement induced by brush deformation play a key role in the cleaning process.

In a previous study [1], experiments were conducted with the brush fully immersed in liquid. However, the liquid movement of PVA brushes in thin liquid film environments—such as those during cleaning—remains unclear. In this study, we investigated how the surrounding liquid level affects cleaning by visualizing liquid movement and measuring flow velocity under varying liquid level conditions during compression—relaxation deformation.

2. EXPERIMENTAL METHOD

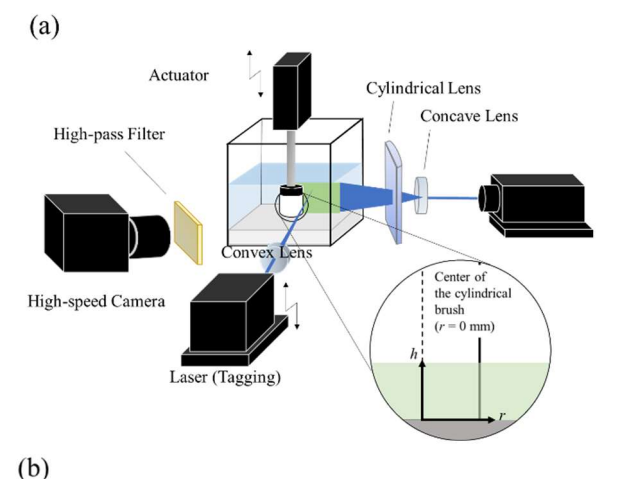
Figure 1(a) shows a schematic of the experimental setup. A cylindrical PVA brush was positioned at the center of a glass water tank, and its indentation

deformation was controlled using a linear actuator. A high-speed camera captured the deformation process.

To visualize the liquid flow induced by brush deformation, the molecular tagging method [2] was employed. We generated a fluorescent region by irradiating a uranine solution with a laser sheet formed by a beam expander and a cylindrical lens. We formed vertical non-fluorescent lines by focusing a tagging laser through a convex lens and moving it vertically across the fluorescent region, as shown in Figure 1(b).

We kept the deformation speed U constant and varied the liquid level h to measure the flow velocity around the brush. During each test, the actuator compressed the brush by 5 mm, held the deformed state for 3 seconds, and then initiated the relaxation motion.

The brush had a diameter of 18 mm and a height of 23 mm. The liquid level h was varied among five conditions: 4, 8, 12, 16, and 25 mm. The deformation speed U was 5 mm/s.



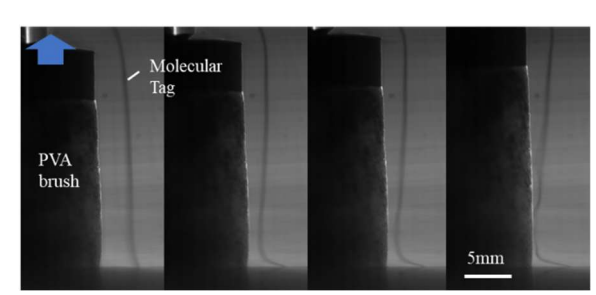


Figure 1 Visualization method of the fluid near the PVA brush: (a) Schematic of the experimental setup; (b) Molecular tags moving with the deformation of the PVA brush.

3. RESULTS AND DISCUSSION

Figure 2 presents composite images of molecular tags at the start and end of compression of the cylindrical PVA brush under different liquid levels. The molecular tags were created on the left side of the PVA brush and moved leftward throughout most of the area except near the bottom surface immediately after compression began. Comparing the displacement of the molecular tags across different liquid levels h, we observed a tendency for greater displacement at lower liquid levels. To quantitatively evaluate this behavior, we calculated the flow velocity of the surrounding liquid from the molecular tag images.

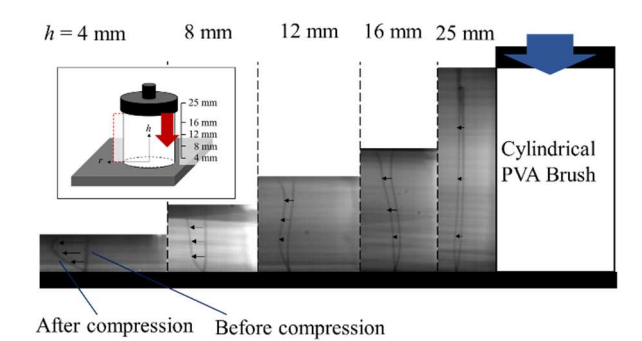


Figure 2 Visualization induced by PVA brush compression during liquid level change with molecular tagging. The figures show a superimposed image of before and after brush compression.

We compare the velocity obtained from image analysis with the theoretical velocity predicted from the continuity equation. The derivation is based on several assumptions regarding the flow symmetry and the behavior of the PVA brush material. Figure 2 shows the coordinates for this consideration. Specifically, the following assumptions were made:

- #1 The flow is axisymmetric, and the velocity components in the vertical (z) and circumferential (θ) directions are negligible $(u_z = u_\theta = 0)$.
- #2 The solid and liquid phases within the sponge move with the same velocity during compression.
- #3 The porosity is uniformly distributed throughout the PVA brush.

When the PVA brush is compressed at a constant velocity U, the volumetric flow rate per unit height, Q is determined from the rate of volume reduction:

$$Q = -\pi R^2 U/h. \tag{1}$$

Assuming incompressible radial flow, the continuity condition requires that the same volumetric flow rate passes through any cylindrical surface of radius r. Thus, the radial velocity u_r at a distance r from the cylinder center is given by:

$$Q = 2\pi r u_r,\tag{2}$$

which yields

$$u_r = Q/2\pi r = -R^2 U/2hr$$
. (3)

This expression describes the radial velocity distribution within the PVA brush during uniform compression under the stated assumptions.

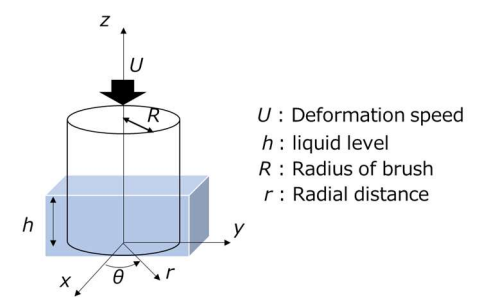


Figure 3 Coordinate and variables for estimating surrounding flow velocity due to porous brush compression.

Figure 4 shows the relationship between the maximum flow velocity u_r during liquid flow-in and flow-out and the liquid level h for the cylindrical brush deformation.

We calculated predicted values and plotted them for comparison. Building on this, Figure 4 illustrates that the flow velocity u_r increases as the liquid level h decreases. This trend agrees with the approximate values derived from the estimation. Comparing the measured u_r during flow-in and flow-out at the same h, the values are identical for h equal to or greater than 8 mm. However, for h=4 mm, the flow velocity during flow-in is slightly higher than during flow-out.

To further discuss these tendencies, we compared and recorded the liquid movement along the side surface of the brush during deformation for h=0 mm. Figure 5 shows images of the brush's side surface during the compression-relaxation process of a fully wetted brush, observed at h=0 mm. During compression, the liquid inside the brush flows down along the side surface as droplets. During relaxation, the liquid that flowed out is fully reabsorbed into the brush, leaving no residual liquid outside. Repeating the compression-relaxation cycle five times produces the same results, indicating that during volume recovery, the brush allows liquid to flow more easily than gas and mainly reabsorbs liquid through the side surface in contact with the liquid phase.

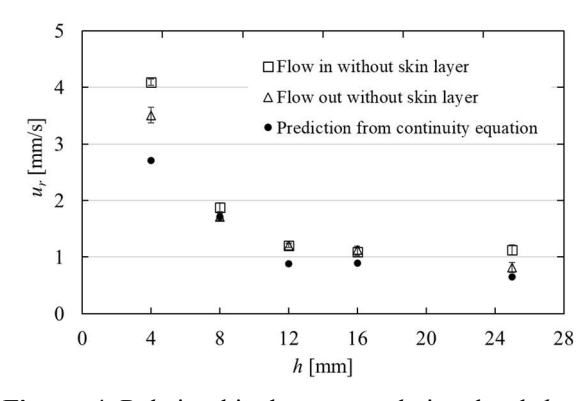


Figure 4 Relationship between solution level h and maximum flow velocity u_r during brush compression

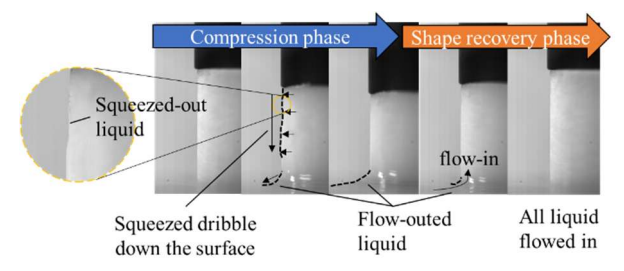


Figure 5 Compression and relaxation of a liquid-filled PVA brush under atmospheric conditions.

4. CONCLUSION

In this study, the liquid movement induced by the deformation of a PVA brush was investigated under various surrounding liquid levels to clarify its role in post-CMP cleaning. Using the molecular tagging method, we successfully visualized the flow-in and flow-out behaviors and quantified the liquid flow velocity during brush compression—relaxation cycles.

The results demonstrated that the liquid velocity around the brush increases as the surrounding liquid level decreases. This tendency is consistent with the approximate estimation derived from the continuity equation. Observations at h=0 mm revealed that liquid expelled during compression was completely reabsorbed during relaxation, indicating that the brush preferentially reabsorbs liquid rather than gas through its side surface.

- [1] Miwa, M. et al., Observation of Liquid Movement during PVA Brush Deformation in Post-CMP Cleaning, ECS J. Solid State Sci. Technol. 14 (2025) No. 2, 024007
- [2] Hosokawa, S. et al., Application of photobleaching molecular tagging velocimetry to turbulent bubbly flow in a square duct, Exp. Fluids 47 (2009) H. 4, S. 745–754.

Primary Breakup Model for Annular Sheet Composed of non-Newtonian Fluid Using Linear Stability Analysis. (11:50~12:10)

*Edin Michael (IIT Hyderabad), Dr. Raja Banerjee.

Abstract

The nonlinearity of the viscous term in the momentum equation poses a challenge to the instability analysis of an annular power-law liquid sheet. In this study, a temporal stability analysis has been carried out for an annular power-law liquid sheet exposed to both inner and outer gas streams. To address the nonlinear viscosity term, a closure parameter in the form of velocity coefficient, g, was introduced, which must be determined from experimental data. High-speed imaging of a pressure swirl atomizer was performed, and the results were used to validate the dispersion equation. An empirical relationship between g and the power law index, n, was established with which the breakup length could be predicted within 13% of the experimental results. It was observed that the application of airflow to either the inner or outer surface of the sheet further destabilized it, with the outer airflow having a stronger impact. The influence of swirl components in the surrounding airflow on the flow instability was also examined. In addition to these, the impact of both the consistency index, K, and the power-law index, n, in the stability of the flow dynamics of the annular sheet was thoroughly investigated. These parameters were found to have a marked impact on the atomization characteristics of power-law fluids in practical applications.

Effect of liquid viscosity on liquid transport in upward vertical annular flow

Bunta Inagaki, Mitsuhiro Fukuta, Toshiyuki Sanada,

Department of Mechanical Engineering, Shizuoka University 3-5-1 Johoku, Naka-ku, Hamamatsu, Shizuoka, 432-8561 JAPAN.

Keywords: Refrigeration cycle, Annular flow, High-viscosity liquid, Liquid transport

ABSTRACT - This study investigates the influence of liquid viscosity on the liquid transport mechanism in vertical upward annular flow. We visualized the flow patterns and determined the wave velocity using the space-time image analysis. We also installed a liquid separation plate at the outlet to measure the mass flow ratios transported by droplet entrainment, the base film, and surface waves, respectively. The result shows that the droplet entrainment rate in water was several percent and almost zero percent in high-viscosity liquid, indicating a minor role. In addition, increasing viscosity suppresses disturbance waves, making ripple waves dominant and that their velocity rises relative to the average film velocity. This suggests that, under high-viscosity conditions, fast ripple waves have a significant influence on liquid transport. This is due to their low liquid film Reynolds number of highly viscous effect and high shear stress at gas-liquid interface of high-speed gas flow.

1. INTRODUCTION

In refrigeration cycles, not only refrigerant but also lubricating oil discharged from the compressor flows through the main components and piping. A reduction in the amount of oil inside the compressor can lead to mechanical failure; therefore, the discharged oil must reliably return to the compressor. In particular, the suction line located between the evaporator and the compressor, liquid oil is transported by the gaseous refrigerant in an annular two-phase flow pattern. However, the transport mechanism of this oil remains poorly understood, and predicting the amount of oil carried by the gas is challenging. In annular two-phase flow, the primary mechanisms of liquid transport include the base film, disturbance waves, and droplet entrainment [1]. For high-viscosity liquids such as oil, however, disturbance wave and droplet generation are suppressed [2] [3]. Moreover, viscosity is expected to hinder the movement of the base film. As a result, strong interfacial shear stress becomes dominant, and surface waves may play a more significant role in transporting the liquid.

This study aims to investigate the influence of gas and liquid properties and their respective flow rates on the liquid transport mechanism, and to develop a method for predicting the transport quantity. To this end, we visualized the flow patterns in a vertical pipe and measured wave velocities. Additionally, we installed a liquid separation plate at the pipe outlet to quantify the liquid flow rates transported by droplets, surface waves, and the base film, respectively.

2. EXPERIMENTAL METHOD AND SETUP

Figure 1 shows a schematic diagram of the experimental apparatus. The main section is 900 mm length of pipe. The distance from the gas-liquid mixing section to the outlet of the pipe is 680 mm. The inner diameter of the pipe D is 18 mm Compressed air was supplied to the center of the pipe through a regulator. Liquid stored in a pressurized tank was supplied to the mixer section, where it was introduced into the pipe through the wall surface via a porous medium.

In measurement section 1 of Fig. 1(a), we measured the liquid film thickness t using optical fiber liquid film sensors [4]. Measurement section 2, located at the outlet of the test pipe, we installed a separation plate. As shown in the enlarged view in Fig. 1(b), we set a plate with a central hole of diameter $D_S = 26$ at a distance $H_S = -10$ mm from the pipe outlet. At liquid outlet 1, we collected liquid with high inertia that had passed through the hole and assumed it was transported by surface waves. At liquid outlet 3, we collected liquid that did not pass through the hole and assumed it was transported by the base film. At liquid outlet 2, we collected droplets that passed through the upper hole along with the gas flow. To measure wave velocity, we recorded the flow patterns between measurement section 1 and the pipe outlet.

The variable flow parameters of this experiment are the liquid viscosity μ_L , the volumetric liquid flow rate Q_L , and gas flow rates Q_G . As the liquid phase, we used water ($\mu_L = 1 \text{ mPa·s}$) and glycerol-water solutions ($\mu_L = 9 \text{ and } 33 \text{ mPa·s}$). We varied Q_L in five conditions from 0.1 to 0.5 L/min in increments of 0.1 L/min. As the gas phase, we used air and varied Q_G in four conditions from 150 to 300 L/min in increments of 50 L/min. Using separation plate, we determined the mass flow rates at three outlet sections by measuring the mass collected per unit time at each outlet: $Q_{L,out1}$ for liquid at outlet 1, $Q_{L,out2}$ for droplet entrainment at outlet 2, and $Q_{L,out3}$ for liquid at outlet 3.

Based on the measurement results, we calculated the averaged liquid film velocity, $V_f = Q_L / \pi t_{ave}D$. And we evaluated the droplet entrainment rate $\xi = Q_{L,out2} / Q_L$, and the liquid flow rate ratio at outlet $1 \ W = Q_{L,out1} / Q_L$. In this experiment, we evaluated the liquid film Reynolds number $Re_L = Q_L / \pi v_L D$, and the gas Reynolds number $Re_G = 4\rho_G Q_G / \pi \mu_G D$ where v_L , ρ_G , and μ_G are the kinematic viscosity of the liquid, gas density, and the gas viscosity, respectively.

To calculate wave velocities, we adopted a spacetime image analysis method. First, we extracted image frames from the experimental video and cropped a specific line (1920×60 pixels) from each frame. These lines were then arranged along the time axis to generate a space-time image. The image captured the trajectories of wave propagation, and we determined the wave velocities by calculating the slope of these trajectories. In this study, we obtained two types of wave velocities, the ripple wave velocity V_W , and the disturbance wave velocity V_D .

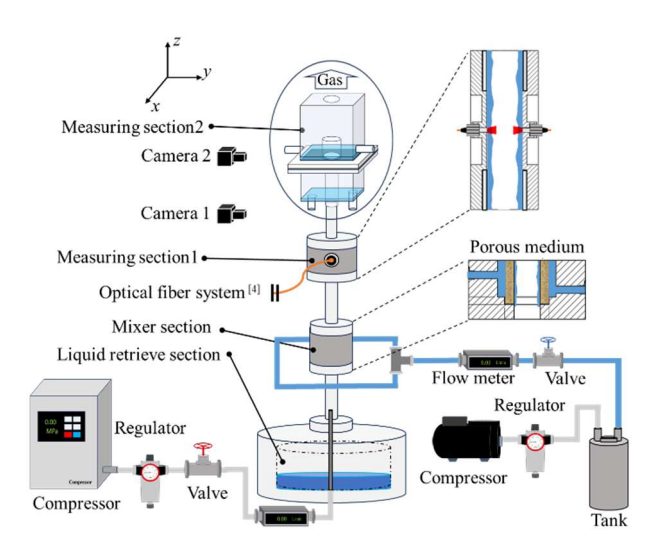


Fig. 1(a) Schematic of experimental setup.

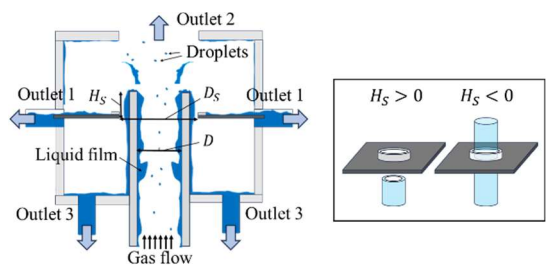


Fig. 1(b) Enlarged view of experimental setup.

3. RESULTS AND DISCUSSION

Figure 2 shows the droplet entrainment rate ξ plotted against Re_G with Re_L represented by a color map. As both Re_G and Re_L increase, the droplet entrainment rate rises, reaching a maximum value of approximately 8 %. This trend is consistent with early empirical correlation indicated by the solid line [5]. In contrast, when the liquid viscosity increases, the present apparatus failed to recover any droplets. These results suggest that, in highly viscous annular flows, droplet entrainment does not play a dominant role in liquid transport.

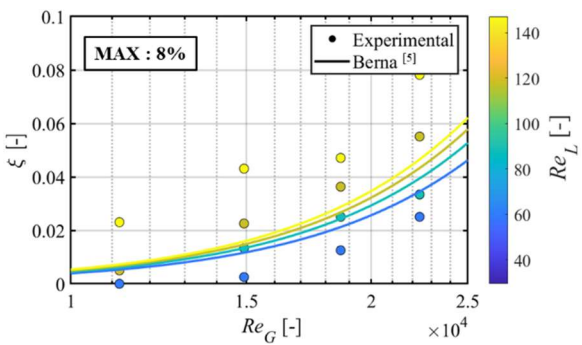


Fig. 2 Droplet dispersion rate ξ ($\mu_L = 1 \text{ mPa} \cdot \text{s}$)

Figure 3 shows the average liquid film thickness t_{ave} plotted against Re_G , with Q_L represented by a color

map. As Re_G increases, t_{ave} tends to decrease. In contrast, increases in μ_L and Q_L lead to an increase in t_{ave} . Notably, the effect of μ_L on t_{ave} is significant. For instance, compared to water, a viscosity of 9 mPa·s results in approximately twice the film thickness, while 33 mPa·s results in a thickness approximately three times greater. Although the viscosity increases by factors of 9 and 33 times, however, indicating that the rate of increase in film thickness does not scale proportionally with viscosity. Next, we calculated and compared the liquid film velocity.

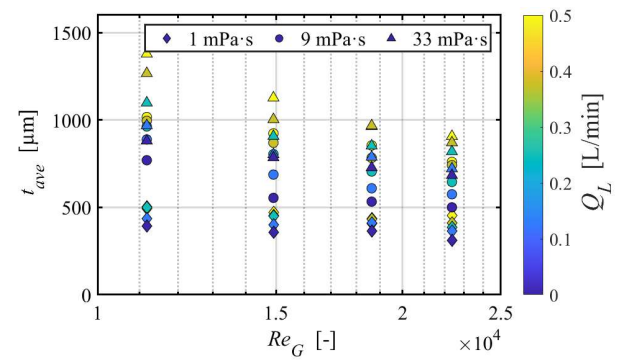


Fig. 3 Effect of liquid viscosity on the averaged liquid film thickness t_{ave} .

Figure 4 shows an example of space-time images of the results for (a) water ($\mu_L = 1 \text{ mPa·s}$) and (b) glycerol-water solution ($\mu_L = 9 \text{ mPa·s}$). In Fig. 4(a), the liquid film thickness measurements revealed unsteady, high-speed waves, indicating the presence of both disturbance waves and ripple waves. At this time, the disturbance wave velocity V_D was approximately five times greater than the average film velocity V_f , while the average ripple wave velocity V_w was about one-third of V_f . On the other hand, in Fig. 4(b), only ripple waves were observed. At this time, V_w was approximately three times greater than V_f . Next, we then analyzed the variation of V_w with respect to flow rate and viscosity parameters, as well as its relationship with V_f .

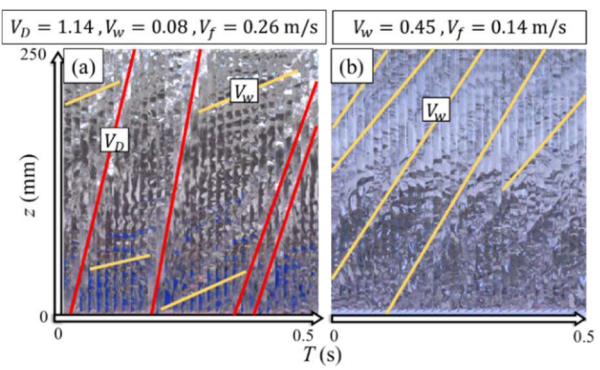


Fig. 4 Visualization result based on a space-time image $(Q_L = 0.4 \text{ L/min}, Q_G = 200 \text{ L/min})$, (a) $\mu_L = 1 \text{ mPa·s}$, (b) $\mu_L = 9 \text{ mPa·s}$.

Figure 5 shows the average ripple wave velocity V_w and plotted against Re_G , with Q_L represented by a color map. In Fig. 5, V_w increases with increasing Re_G . Additionally, higher liquid viscosity leads to greater V_w showing values approximately 4 to 6 times larger than those for water.

Figure 6 shows the ratio of average film velocity V_f

to V_w , plotted against Re_G , with Q_L represented by a color map. In Fig.6, for liquids with the same viscosity, the velocity ratio V_w / V_f shows little variation with increasing Re_G . This is because as Re_G increases, t_{ave} decreases and V_f increases, while V_w also increases simultaneously. On the other hand, increasing liquid viscosity led to an overall rise in V_w / V_f . For instance, compared to water, V_w / V_f was approximately four times greater at 9 mPa·s and about ten times greater at 33 mPa·s. In this case, although the viscosity increased by a factor of 33, t_{ave} only increased by a factor of 2 to 3, and V_f did not decrease significantly. However, Re_L dropped substantially, indicating that the influence of viscosity becomes more pronounced. Since V_w increases with liquid viscosity, we expect the velocity gradient near the wall to decrease, allowing the base liquid film to remain in near wall, while a significant portion of the liquid is transported by the ripple waves.

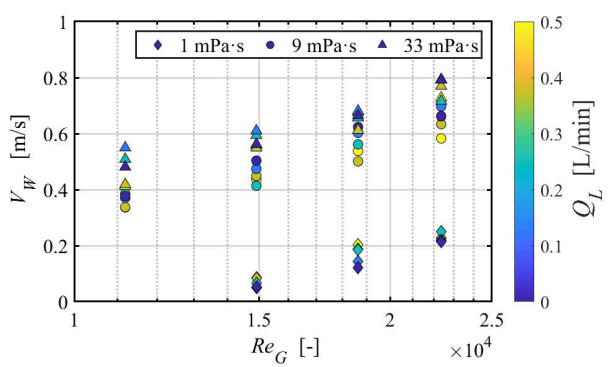


Fig. 5 Effect of liquid viscosity on the ripple wave velocity V_w ,

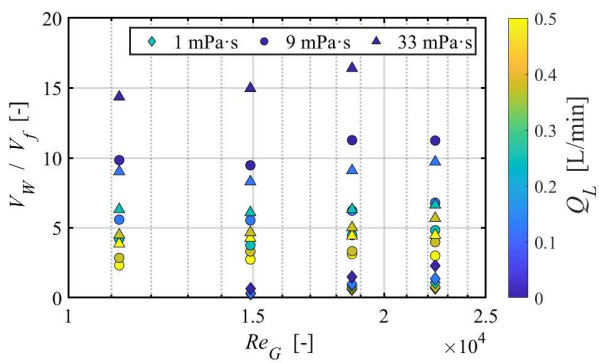


Fig. 6 Effect of liquid viscosity on the velocity ratio V_w / V_f

Figure 7 shows the results of the liquid mass flow rate ratio W for (a) water, (b) glycerol-water solution ($\mu_L = 33$ mPa·s). In case (a), W tended to decrease with increasing Re_G in the low Q_L . In contrast, in case (b), W increased with increasing Re_G . These results indicate that W increases with increasing V_W for high-viscous liquids. Additionally, the range of W values for a given Re_G narrowed as the viscosity increased. These results imply that larger W values are obtained when Q_L is low and the velocity ratio V_W / V_f is high. These results suggest that, in the case of high-viscosity liquids, fast-moving ripple waves may play a significant role in liquid transport. We hypothesize that this behavior arises from a combination of two factors: (1) the strong viscous effects experienced by low-Reynolds-

number liquid films near the wall due to their high viscosity, and (2) the high interfacial shear stress generated by the gas phase, which have a very high Reynolds number.

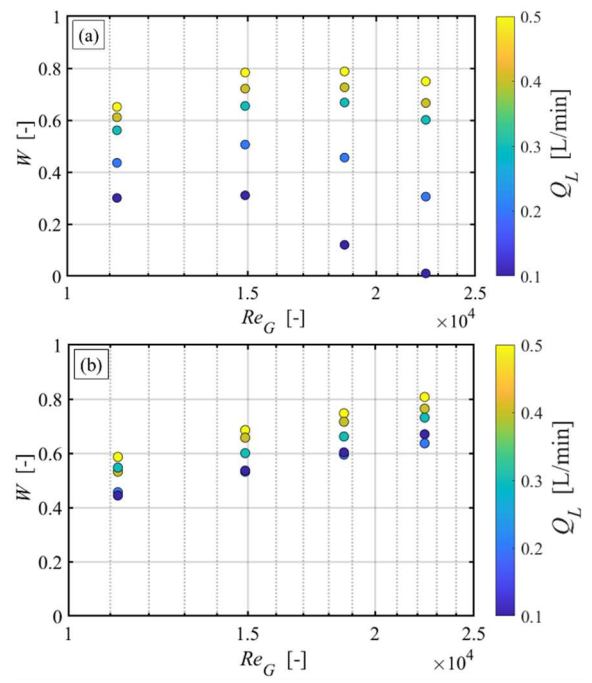


Fig. 7 Effect of liquid viscosity on the ratio *W* between liquid flow rate corrected by outlet 1 $Q_{L,out1}$, and entire flow rate Q_L (a) $\mu_L = 1$ mPa·s, (b) $\mu_L = 33$ mPa·s

4. CONCLUSION

In this study, we investigated the influence of high-viscosity liquids on liquid transport in vertical upward annular flow. We clarified that droplet entrainment is not a dominant factor in the transport of high-viscosity liquids. Under high-viscosity conditions, we suggest that accelerated ripple waves may play a significant role in transporting the liquid.

- [1] Le Corre, J. M., "Phenomenological model of disturbance waves in annular two-phase flow," *Int. J. Multiphase Flow*, 151, 104057, (2022).
- [2] Fukano, T. and Furukawa, T., "Prediction of the effects of liquid viscosity on interfacial shear stress and frictional pressure drop in vertical upward gasliquid annular flow," *Int. J. Multiphase Flow*, 24(4), pp. 587-60 3, (1998).
- [3] Watanabe, S., Mizushima, Y. and Sanada, T., "Thin liquid film thickness measurement using stepped-index-type optical fiber sensors," *J. Fluid Sci. Tech.*, 19(2), JFST0007, (2024).
- [4] Wang, Z. et al., "Research on the effects of liquid viscosity on droplet size in vertical gas-liquid annular flows," *Chemical Engineering Science*, Vol. **220**, (2020), 115621
- [5] Berna, C., Escriva, A., Munoz-Cobo, J. L. and Herranz, L. E., "Review of droplet entrainment in annular flow: Characterization of the entrained droplets," *Progress in Nuclear Energy*, 79, pp. 64-86, (2015).

Numerical simulation of liquid film thickness distribution and liquid replacement on a rotating disk

Jukiya Ikegaya, Shinsuke Watanabe, Toshiyuki Sanada

Department of Mechanical Engineering, Shizuoka University 3-5-1 Johoku, Chuo-ku, Hamamatsu, Shizuoka, 432-8561 JAPAN.

Keywords: Liquid film thickness, Liquid replacement, Rotating Disk, OpenFOAM

ABSTRACT – Liquid film flow on rotating disk plays an important role in industrial fields. To better understand how chemical solution reaches and spreads across the disk surface, we investigated both the liquid-film thickness distribution and the concentration transport within the liquid film using OpenFOAM. As a result, the simulations result of liquid film thickness distribution and theoretical model showed good overall agreement. We also reproduced the replacement process in which an incoming liquid spreads over and displaces an existing film.

1. INTRODUCTION

Processes that utilize liquid film flow on rotating disks appear widely across industrial fields. Spinning disk reactors (SDRs) represent one example of this industrial processes [1]. Nanoparticle production in SDRs relies on precipitation reactions, and improving the efficiency of this process requires producing uniform nanoparticles at a high rate. Recent approaches supply chemical solution onto a rotating disk and activate or control the precipitation reaction through the shear force generated between the liquid film and the disk surface. Achieving high efficiency in this process therefore requires a detailed understanding of the flow characteristics of the formed liquid film.

Liquid film flow on rotating disk also plays an important role in semiconductor cleaning processes. In single-wafer cleaning, a representative example, a cleaning solution is supplied onto a rotating wafer, and the resulting liquid film serves as a reaction field for surface cleaning. Because the chemical solution delivered to the surface strongly influences cleaning performance, it is essential to quantitatively understand how effectively the incoming solution can replace the existing liquid on the wafer [2].

In this study, we focus on the liquid film flow formed on a rotating disk and aim to clarify its flow characteristics. To achieve this, we use the finite-volume-based software OpenFOAM [3] and simulated the liquid film flow. Through these simulations, we reveal the liquid replacement behavior within the film under various flow conditions.

2. EXPERIMENTAL METHOD

We used OpenFOAM to solve the thin-film flow formed over the rotating disk by the liquid jet ejected from a nozzle in this study. Moreover, we implemented a method in OpenFOAM that computes the convection (explicitly determined by the fluid flow) and diffusion of solute transported by the liquid jet. The following paragraphs describe these methods in detail. We

computed the film flow formed by the injected liquid jet using interFoam, an incompressible gas—liquid two-phase flow solver in OpenFOAM. In interFoam, a modified volume-of-fluid (VOF) method captures the motion of the gas—liquid interface. This method includes a compressive velocity term that prevents the interface from becoming smeared.

$$\frac{\partial \alpha}{\partial t} + \nabla \cdot (\alpha u) + \nabla \cdot \{u_x \alpha (1 - \alpha)\} = 0 \ (1)$$

where t is the time, u is the fluid velocity, and u_x is the relative velocity between gas and liquid phases. Since $\alpha(1)$ $-\alpha$) appears, the third term in Eq. (1) is zero except for the computational cells at the interface. The term works such that the interface is maintained sharp. The mass and momentum conservation equations are coupled by the PIMPLE algorithm, which combines the PISO [4] and SIMPLE algorithms [5]. The surface tension is taken into account as a body force in the computational cells containing the interface by the continuous surface force method. In this study, we assumed that chemical species exist only in the liquid phase. The distribution of the solute concentration obeys the advective-diffusive equation in which the advection velocity is explicitly determined by the fluid velocity field. When the advection-diffusion equation is simply solved, some amount of the solute passes through the interface and leaks into the gas phase in the transport process. Thus, in the present paper, the following Eq. (2) is solved.

$$\frac{\partial \alpha C}{\partial t} + \nabla \cdot (\alpha C u) = \nabla \cdot (\alpha D \nabla C) \tag{2}$$

where C is the solution concentration and D is the diffusivity of the solute liquid. This corresponds to making the amount of the solute passing through the interface in each computational cell zero. By implementing this equation in interFoam, we can compute the advection and diffusion of the solute only in the liquid. We developed this implementation following the framework of a multiphase CFD solver. In this study, we simulate liquid film flow on a rotating disk and conducted analyzing the replacement process between two liquids with different concentrations.

3. RESULTS AND DISCUSSION

Figure 1 illustrates a graph where the horizontal axis represents the distance from disk center r, and the vertical axis represents the liquid film thickness h. These results reflect a disk rotation speed ω of 100 and 200 rpm and water flow rates Q_w of 0.5 L/min. The radius of rotating

disk is 40 mm. The plotted points illustrate the simulation results. The solid and dashed lines illustrate the liquid film models for single-liquid jet impingement on a rotating disk: the Nusselt and the Pigford models [6]. The Nusselt model is represented by Eq. (3), while Eq. (4) and (5) define the Pigford model.

$$h = \left(\frac{3Q_W \nu}{2\pi r^2 \omega^2}\right)^{\frac{1}{3}} \tag{3}$$

$$u\frac{\partial u_r}{\partial r} - \frac{u_{\theta}^2}{r} = -\frac{12\pi^2 r^2 K_1 \nu}{\varrho_w^2} u_r^3$$
 (4)

$$u\frac{\partial u_{\theta}}{\partial r} + \frac{u_{r}u_{\theta}}{r} = \frac{12\pi^{2}r^{2}K_{2}v}{Q_{w}^{2}}u_{r}^{2}(r\omega - u_{\theta}) \quad (5)$$

Here, the kinematic viscosity of water is noted as v, the radial velocity is denoted as u_r , and the circumferential velocity component is represented as u_θ . The coefficients, K_1 and K_2 [7], were estimated from Burns et al. In the Pigford model, the liquid film thickness is determined using the radial velocity u_r , which is obtained from Equations (4) and (5) and is calculated based on the continuity equation $h = Q_w/2\pi x u_r$.

Our simulation results show good overall agreement with the theoretical model. At 100 rpm, the liquid-film thickness distribution closely follows the Pigford model. prediction across the entire radial region. At 200 rpm, the simulation still aligns well with the Pigford model, but we observe noticeable deviations near the disk edge. Conversely, the result asymptotically approaches the Nusselt model as r increases. These results demonstrate that this solver can resolve the liquid-film thickness distribution on a rotating disk with sufficient accuracy.

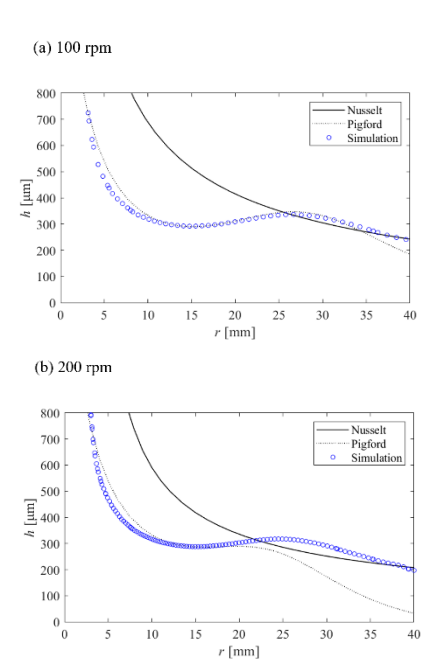


Figure 1 Comparison of liquid film thickness between theoretical model and simulation.

Next, we simulated the replacement of an existing liquid film on the rotating disk by a newly supplied liquid with a different concentration. Figure 2(a) shows the state before the inflow (t=0 s), and Figure 2(b) shows the state at t=1 s. In this case, we set the concentration of the incoming liquid to C=1 and that of the existing film to C=0.5. The result reflects a disk rotation speed ω of 100 rpm and water flow rates Q_w of 1 L/min. The radius of rotating disk is 80 mm. As a result, we successfully reproduced the replacement process between the two liquids with different concentrations. Also, we showed that the existing liquid film was completely replaced by the incoming liquid within one second.

In future work, we will investigate how changes in rotation speed, flow rate, and concentration influence the replacement process and identify the conditions that optimize the treatment. In addition, because the present mesh remains relatively coarse, we plan to perform simulations with finer meshes to more accurately resolve the concentration gradients.



Figure 2 Liquid replacement on a rotating disk.

4. SUMMARY

This study used OpenFOAM to analyze liquid film flow on a rotating disk. The simulated film thickness showed good agreement with the theoretical model. We also reproduced the replacement of an existing film by an incoming liquid with a different concentration. These results confirm that interFoam solver in OpenFOAM can effectively capture both film formation and concentration transport on rotating disk.

- [1] D. Wang, et al. Chem. Eng., 390 (2020) 124392.
- [2] K.Kaneko, et al. ECS Transactions 2.6 (2007) 295.
- [3] C. J. Greenshields, OpenFOAM User Guide version9, OpenFOAM Foundation Ltd, (2021).
- [4] R. I. Issa, et al. J. Comp. Phys., 62 (1986) 66.
- [5] S. V. Patankar, et al. Int. J. Heat Mass Transfer, 15 (1972) 1787.
- [6] R. M. Wood, et al., Trans. Inst. Chem. Eng., 51 (1973) 315.
- [7] J. R. Burns, et al., Chem. Eng. Sci., 58 (2003) 2245.

Laboratory Exchange Program (SSSV)Indian Institute of Technology Hyderabad, 21st Nov 2025

Study of the Atmospheric Boundary Layer Flow over a Stripe/Band heterogeneity. (14:20~14:40)

*Kingshuk Mondal (IIT Hyderabad), Niranjan Ghaisas.

Abstract

The atmospheric boundary layer (ABL), governed by shear, buoyancy, Coriolis forces, and surface forcing, plays a key role in modulating weather, air quality, and wind energy. This study investigates the influence of stripe- or band-type surface-roughness heterogeneity on neutral ABL flow. The turbulence statistics downstream of the stripe exhibit features of both smooth-to-rough and rough-to-smooth transitions and show strong sensitivity to the stripe length (L_B). An internal boundary layer (IBL) forms downstream of the trailing edge of the stripe and remains largely insensitive to variations in L_B. The IBL height is then used as an input to models for the streamwise velocity and turbulence intensity (TI). The velocity model is purely kinematic and extends the framework of Ghaisas (2020) for a single roughness transition. Likewise, the weighted-average TI model for a single transition is adapted for the stripe case and yields acceptable predictions in the vicinity of the stripe.

Self-propelling microswimmers near the corners of a confined meniscus: Attraction, trapping, and escape. (14:40~15:00)

*Subhasish Guchhait, Harshita Tiwari (IIT Madras), Sumesh P.Thampi(IIT Madras), Ranabir Dey

Abstract

In a viscous dominant region where the role of inertia is significantly less, the biological microswimmer, i.e., bacteria, algae, protozoa, usually deals with critical environments such as curved fluid-fluid interface, grove or corner regions, etc., for their survival and growth. They adopt different swimming strategies to deal with these environments, which is an inspiration to explore the role of fluid mechanics in such interactions. So far, very few research works have been done on artificial microswimmers in the vicinity of such environments, specifically in confined environments. In our recent study, experimentally, we successfully explored the dynamics of self-propelled microswimmers (active pusher CB15 oil droplets) near the air-water and oil-water interface inside microchannels (10:1 PDMS), specifically near the corner. Using bright-field microscopy and in-house MATLAB code, we track the instantaneous centroid trajectory of the droplet over time, which helps us to calculate different velocity components, residence time at various locations near the interface, etc. We define the corner effect, α_c , by the ratio of half-channel width to the square root of the multiplication droplet radius and interface radius. As α_c increases, the corner attraction increases, and the residence time at the corner increases. We observe that these droplets exhibit a monopolar swimming pattern at the corner. To get a better understanding of this interaction, we use the image system technique, and numerically, we use the Lattice-Boltzmann technique. We observe that the attraction of a free interface corner is comparatively higher than that of a solid-solid corner. These studies will help to understand the interaction of artificial droplets with biological cells, tissues, mucus, etc., and will contribute towards medical applications such as targeted cargo and drug delivery systems.

Laboratory Exchange Program (SSSV)Indian Institute of Technology Hyderabad, 21st Nov 2025

Hydrodynamics of a falling plate.

*Om Godse (IIT Hyderabad), Vandan Chavan (IIT Hyderabad), Minori Hamate(Tokyo University of Agriculture and Technology), Yoshiyuki Tagawa(Tokyo University of Agriculture and Technology) & Harish Dixit

Abstract

When an object falls toward a flat surface, the motion is not simply a collision event but may be significantly affected by the thin air film formed between the object and the surface. This air film can reduce friction and impact forces, allowing for a smoother sinking motion. If the mass of the object is small enough, it may even lose contact with the surface and glide before crashing down. In this work, we investigate this phenomenon for a falling plate, using lubrication theory to simplify the Navier Stokes equations and obtain an analytical expression for the pressure distribution in the air film, which we then use to compute the plate's motion over time. We compare these theoretical predictions with experimental data obtained from a high speed camera, and find good agreement between both.